DES 2018-0326
FERMILAB-PUB-19-103-AE

Mon. Not. R. Astron. Soc. **000**, 1–?? (2019) Printed 22 March 2019 (MN LaTeX style file v2.2)

Stellar mass as a galaxy cluster mass proxy: application to the Dark Energy Survey redMaPPer clusters

A. Palmese[1,2⋆], J. Annis[1], J. Burgad[3], A. Farahi[4], M. Soares-Santos[5], B. Welch[6], M. da Silva Pereira[5], H. Lin[1], S. Bhargava[7], D. L. Hollowood[8], R. Wilkinson[7], P. Giles[7], T. Jeltema[8,8], A. K. Romer[7], A. E. Evrard[9,10], M. Hilton[11], C. Vergara Cervantes[7], A. Bermeo[7], J. Mayers[7,7], J. DeRose[12,13], D. Gruen[12,13,14], W. G. Hartley[2,15], O. Lahav[2], B. Leistedt[16], T. McClintock[17], E. Rozo[17], E. S. Rykoff[13,14], T. N. Varga[18,19], R. H. Wechsler[12,13,14], Y. Zhang[1], S. Avila[20], D. Brooks[2], E. Buckley-Geer[1], D. L. Burke[13,14], A. Carnero Rosell[21,22], M. Carrasco Kind[23,24], J. Carretero[25], F. J. Castander[26,27], C. Collins[28], L. N. da Costa[22,29], S. Desai[30], J. De Vicente[21], H. T. Diehl[1], J. P. Dietrich[31,32], P. Doel[2], B. Flaugher[1], P. Fosalba[26,27], J. Frieman[1,6], J. García-Bellido[33], D. W. Gerdes[9,10], R. A. Gruendl[23,24], J. Gschwend[22,29], G. Gutierrez[1], K. Honscheid[34,35], D. J. James[36], E. Krause[37], K. Kuehn[38], N. Kuropatkin[1], A. Liddle[39], M. Lima[40,22], M. A. G. Maia[22,29], R. G. Mann[41], J. L. Marshall[42], F. Menanteau[23,24], R. Miquel[43,25], R. L. C. Ogando[22,29], A. A. Plazas[44], A. Roodman[13,14], P. Rooney[7], M. Sahlen[45], E. Sanchez[21], V. Scarpine[1], M. Schubnell[10], S. Serrano[26,27], I. Sevilla-Noarbe[21], F. Sobreira[46,22], J. Stott[47], E. Suchyta[48], M. E. C. Swanson[24], G. Tarle[10], D. Thomas[20], D. L. Tucker[1], P. T. P. Viana[49,50], V. Vikram[51], A. R. Walker[52]

(DES Collaboration)

(Affiliations are listed at the end of paper)

22 March 2019

ABSTRACT

We introduce a galaxy cluster mass observable, $\mu_\star$, based on the stellar masses of cluster members, and we present results for the Dark Energy Survey (DES) Year 1 observations. Stellar masses are computed using a Bayesian Model Averaging method, and are validated for DES data using simulations and COSMOS data. We show that $\mu_\star$ works as a promising mass proxy by comparing our predictions to X–ray measurements. We measure the X–ray temperature–$\mu_\star$ relation for a total of 150 clusters matched between the wide–field DES Year 1 redMaPPer catalogue and *Chandra* and *XMM* archival observations, spanning the redshift range $0.1 < z < 0.7$. For a scaling relation which is linear in logarithmic space, we find a slope of $\alpha = 0.488 \pm 0.043$ and a scatter in the X–ray temperature at fixed $\mu_\star$ of $\sigma_{\ln T_X|\mu_\star} = 0.266^{+0.019}_{-0.020}$ for the joint sample. By using the halo mass scaling relations of the X–ray temperature from the Weighing the Giants program, we further derive the $\mu_\star$–conditioned scatter in mass, finding $\sigma_{\ln M|\mu_\star} = 0.26^{+0.15}_{-0.10}$. These results are competitive with well–established cluster mass proxies used for cosmological analyses, showing that $\mu_\star$ can be used as a reliable and physically motivated mass proxy to derive cosmological constraints.

Key words: galaxies: clusters: general – galaxies: evolution – galaxies: halos – cosmology: observations – surveys.

1 INTRODUCTION

Galaxy clusters are fundamental cosmological probes for large galaxy surveys such as the Dark Energy Survey (DES; The Dark Energy Survey Collaboration 2005). The estima-

⋆ E-mail: palmese@fnal.gov

tion of the cosmological parameters from clusters abundance is allowed by the dependence of the dark matter halo mass function on cosmology (Press & Schechter 1974; Sheth & Tormen 2002; Tinker et al. 2008), but it requires estimates of cluster total masses from the observables of our galaxy survey. In practice, we seek cluster mass observables (or mass proxies) that tightly correlate with the dark matter halo mass.[1] In other words they exhibit a low scatter in halo mass at fixed mass proxy (and vice versa).

Several cluster finders are based on the cluster red-sequence (e.g. Koester et al. 2007; Hao et al. 2010; Oguri 2014; Rykoff et al. 2014). Amongst those, redMaPPer (Rykoff et al. 2014) has been extensively studied and its mass proxy, the richness λ, calibrated for large photometric surveys such as the Sloan Digital Sky Survey (SDSS) and the DES over the past decade (Rozo et al. 2009a,b, 2011; Rykoff et al. 2016; Melchior et al. 2016; Simet et al. 2017; Costanzi et al. 2019). On the other hand, there exists broad evidence that the content of clusters includes a non–negligible fraction of bluer, star–forming galaxies that do not follow the red sequence colour–magnitude relation, in particular towards increasing redshift (Oemler 1974; Butcher & Oemler 1978; Butcher & Oemler 1984; Donahue et al. 2002; Zhang et al. 2017). This effect is known as the Butcher–Oemler effect. Whether the inclusion of the blue cloud can improve cluster mass estimates for cosmology is a matter of debate (e.g. Rozo et al. 2011) and depends on the survey characteristics. At higher redshifts, the blue fraction becomes more significant (though it can also reach $\sim 30\%$ below redshift ~ 0.3; Zu & Mandelbaum 2016) and the red sequence is not as distinguishable in colour-magnitude space as at lower redshift. In these regimes, the inclusion of the bluer members may play a significant role in cluster abundance studies of DES and other on–going and future photometric surveys (the Large Synoptic Sky Telescope, LSST, Ivezić et al. 2008; Euclid, Laureijs et al. 2011) that push towards higher redshifts, $z = 1$ and beyond.

One clear advantage of including blue galaxies in cluster catalogues is in studying cluster properties and their evolution with redshift, in particular the Butcher-Oemler effect and quenching mechanisms. Moreover, cluster finders able to identify also cluster members that do not belong to the red sequence (Miller et al. 2005; Soares-Santos et al. 2011) already exist. For these reasons, we develop a low–scatter mass proxy for cluster finders that is not red-sequence based.

Previous works (for example, Andreon 2012) have exploited stellar masses as a possible cluster mass proxy. We here extend those studies by using a larger sample of X–ray clusters for calibration and by complementing the stellar mass estimates with a membership probability scheme presented in a companion paper, Welch et al. (2019). A feasibility study for stellar mass computation with DES data has already been carried out in Palmese et al. (2016), where they found that stellar masses of clusters members can be recovered within 25% of Hubble Space Telescope Cluster Lensing and Supernovae Survey with Hubble (CLASH) values. The use of the stellar mass content as a probe of total cluster mass is empirically but also physically motivated by the stellar–to–halo connection (see e.g. Wechsler & Tinker 2018 for a review), which follows a linear relation in the logarithm of masses at the clusters scales. An analysis of the scaling relation for $\mu_\star$ with halo mass thus has interesting implications not only for cosmological analysis, but also for the stellar–to–halo mass relation (SHMR), which is of interest to understand galaxy evolution within clusters (see Palmese et al. 2019 for implications on the SHMR from the whole DES redMaPPer sample). In fact, the SHMR can be expressed as a joint likelihood of mass and observable properties. Because of this, the stellar mass can potentially be more tightly related to the total mass of clusters on the individual halo basis, than number counts would. On the other hand, projection effects due to foreground and background galaxies being confused with cluster members, are perhaps one of the most problematic issue in cluster cosmology with richness (Costanzi et al. 2019). These effects are likely to affect our stellar mass observable in a very similar way to λ, because of the similarities between the two methods.

We therefore apply our method to a well–established cluster catalogue, the DES Year 1 (Y1) redMaPPer catalogue, matched to X–ray observations. Nevertheless, this mass proxy can easily be used with other, non–red–sequence based, cluster finders. We also test our cluster stellar mass estimates against simulations.

The X–ray temperature and luminosity of clusters represent a well–known, low scatter mass proxy for cluster mass, for which total mass scaling relations have been studied in depth (e.g. Mantz et al. 2016). The formalism by Evrard et al. (2014) allows us to link the scaling relations of different mass proxies when a lognormal covariance is assumed around the mean scaling relations of the mass proxies. It is thus possible to derive an estimate of the scatter on the total mass of clusters by using the scaling relations between our mass proxy and the X–ray temperature, and between the X–ray temperature and the total mass of clusters. Such estimates provide essential prior information for our mass proxy–mass scatter in a cosmological analysis with cluster abundance.

In this work we present a stellar mass–based cluster mass proxy, called $\mu_\star$, and assess its performance as a mass proxy using archival X–ray data. This paper is divided into five sections. In Section 2 we describe the DES galaxy catalogue, the Y1 redMaPPer catalogue and the X–ray cluster catalogues used. In Section 3 we present a new method to compute galaxy stellar masses, that uses a Bayesian model averaging technique. We then introduce the scheme to produce our stellar mass proxy $\mu_\star$ and briefly describe the membership probability assignment. We also present the method used to compute the X–ray scaling relations and the mass scatter. Section 4 contains measurements of the $T_X - \mu_\star$ relation and scatter constraints, both for the temperature scatter and the total cluster mass scatter. Section 5 contains discussion and conclusions.

Throughout this work we assume a ΛCDM flat cosmology with $h = 0.7$, $\Omega_m = 0.3$, $\Omega_\Lambda = 0.7$. The notation adopted for the cluster mass and radius follows the one often used in the literature. The radii of spheres around the cluster centre are written as $r_{\Delta m}$ and $r_{\Delta c}$ where Δ is the overdensity of the sphere with respect to the mean matter density (subscript m) or the critical density (subscript c) at the cluster redshift. Masses inside those spheres are therefore

[1] In the following, we refer to the dark matter halo mass as halo mass for brevity.

$M_{\Delta m} = \Delta \frac{4\pi}{3} r^3_{\Delta m} \rho_m$ and similarly for $M_{\Delta c}$. In the following, we quote $\Delta = 200$, which roughly corresponds to the density contrast at virialisation for a dark matter halo at $z = 0$. Logarithms indicated as ln are in base e, and Log are in base 10. Errors are 68% confidence level unless otherwise stated.

2 DATA

2.1 DES Year 1 data

The DES[2] is an optical-near-infrared survey that imaged 5000 deg^2 of the South Galactic Cap in the *grizY* bands over 575 nights spanning almost six years. The survey was carried out using a ~ 3 deg^2 CCD camera (the DECam, see Flaugher et al. 2015) mounted on the Blanco 4-m telescope at the Cerro Tololo Inter-American Observatory (CTIO) in Chile. DES started in 2012 with a testing period (November 2012 – February 2013) called DES Science Verification (SV)[3]. The data used here come from the first year of observations (September 2013 – February 2014, Diehl et al. 2014) and cover $1,839$ deg^2 with up to 4 passes per filter. The data are available at `http://des.ncsa.illinois.edu/releases/y1a1`.

The survey strategy is designed to optimize the photometric calibration by tiling each region of the survey with several overlapping pointings in each band. This provides uniformity of coverage and control of systematic photometric errors. This strategy allows DES to determine photometric redshifts of $\sim$ 300 million galaxies to an accuracy of $\sigma(z) \simeq 0.07$ out to $z \gtrsim 1$, with some dependence on redshift and galaxy type, and cluster photometric redshifts to $\sigma(z) \sim 0.02$ or better out to $z \simeq 1.3$ (The Dark Energy Survey Collaboration 2005). It has already found ~ 400 million objects, including stars and galaxies, from the first three years of operations (Abbott et al. 2018), and $\sim 80,000$ galaxy clusters from the first year.

The DES Data Management (DESDM) pipeline was used for data reduction, as described in detail in Sevilla et al. (2011), Desai et al. (2012) and Mohr et al. (2012). The process includes calibration of the single-epoch images, which are co-added after background subtraction and then cut into tiles. The source catalogue was created using Source Extractor (SExtractor, Bertin & Arnouts 1996) to detect objects on the *riz* co-added images. The median 10σ limiting magnitudes of Y1 data for galaxies are $g = 23.4$, $r = 23.2$, $i = 22.5$, $z = 21.8$, and $Y = 20.1$. Drlica-Wagner et al. (2018) made further selections to produce a high-quality object catalogue called the Y1A1 "gold" catalogue.

The cluster catalogue used here is the cosmology Y1 redMaPPer catalogue v6.4.14 with richness $\lambda > 5$, which consists of 87,297 clusters. This sample is then matched to archival X–ray observations from *Chandra* and *XMM*. The 2D distribution of richness and redshift of the matched samples is shown in Figure 1. The centre position (given by the galaxy with the highest central probability p_{cen}) and the cluster redshift are the only outputs used from this catalogue. The galaxies associated with each cluster are taken from the Y1A1 gold catalogue. We select objects with `MODEST_CLASS`=1 in order to exclude sources that are likely not to be galaxies.

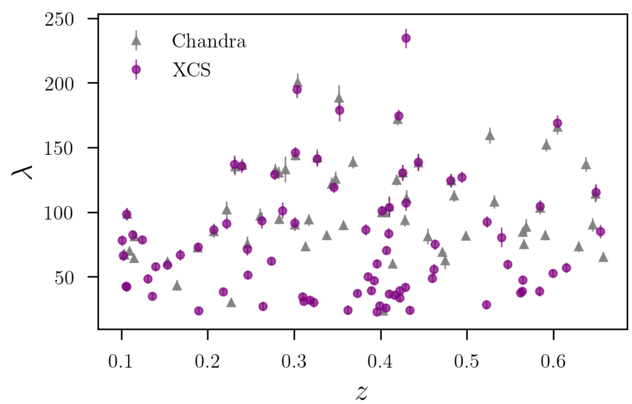

Figure 1. Distribution in richness λ and redshift for the DES Year 1 redMaPPer clusters matched to *Chandra* and *XMM* archival data using the methods presented in Hollowood et al. (2018) and Giles et al. (2019).

While the cluster catalogue is based on Y1 data, the photometry comes from the deeper Year 3 data (median 10σ coadded catalogue depths for a $1.95''$ diameter aperture: $g = 24.33$, $r = 24.08$, $i = 23.44$, $z = 22.69$, and $Y = 21.44$ mag; Abbott et al. 2018). The photometry is the result of the Multi-Object Fitting (MOF) pipeline that uses the `ngmix` code.[4]

In order to compute the membership probabilities (as described in Section 3.2), we use photometric redshifts (photo-z's) from the template-based Bayesian Photometric Redshifts (BPZ) algorithm (Benítez 2000). The catalog used in this work uses the same procedure as outlined in Hoyle et al. (2018). Briefly, six basic templates taken from Coleman, Wu & Weedman (1980) and Kinney et al. (1996) were corrected for redshift evolution and any residual calibration errors. Corrections were performed via finding the best-fit template for a subset of the PRIMUS spectroscopic data set (Cool et al. 2013) and computing median offsets between the observed photometry and template predictions within each template type, in a sliding redshift interval, $\Delta z = 0.06$. The magnitude and galaxy type redshift prior was then calibrated using the COSMOS+UltraVISTA photometric redshift catalogue of Laigle et al. (2016). Our BPZ run produces redshift probability distributions for $0 < z < 3.5$ in steps of $dz = 0.01$. We use the mean of the probability distribution function (PDF) and an estimate of the width of the PDF: Welch et al. (2019) show that this is a good enough approximation to estimate membership probabilities with our method. The member galaxy properties are instead computed assuming the much more precise cluster redshift.

[2] `www.darkenergysurvey.org`
[3] For public data release see: `http://des.ncsa.illinois.edu/releases/sva1`
[4] `https://github.com/esheldon/ngmix`

2.1.1 *Completeness of the stellar mass sample*

The galaxy sample described in Section 2.1 is cut in r-band absolute magnitude. Absolute magnitudes were estimated using K-corrections computed from galaxy templates generated by `kcorrect` v4.2 (Blanton & Roweis 2007). We took each galaxy's redshift to be the same as its photo-z, found the closest `kcorrect` template on a grid of redshift and colors ($g-r$, $r-i$, and $i-z$), and used that template's K-correction from observed i-band to rest-frame r-band to calculate M_r. An absolute magnitude cut M_r brighter than -19.8 was then applied to the galaxy catalog. This cut ensures that our galaxy sample is volume limited across the redshift range considered. In Figure 2 we show the observed r-band magnitudes that the galaxies in our sample would have if they had an absolute magnitude $M_r = -19.8$ as a function of redshift. These are computed using the K-corrections and distance modulus output by our galaxy Spectral Energy Distribution (SED) fitting code using Bayesian Model Averaging (BMA; described in Section 3) for galaxies with a membership probability $> 15\%$ (corresponding to the median of the membership probability distribution), in order to be representative of a realistic cluster galaxy population. We show that the $90^{\rm th}$ percentile of the distribution in redshift bins is below the 95% completeness limit of the DES Y1A1 gold catalog (22.9 in $i-$band) over the redshift range covered by the redMaPPer cosmology catalog. We compare to the Y1 magnitude limit as our galaxy catalog contains objects detected in Y1, even if they are matched to the deeper Y3 photometry. We can conclude that with the chosen cut we are $\sim 90\%$ complete.

In order to estimate the completeness in stellar mass, we look at the mass $M_\star^{lim}$ each galaxy would have, at its redshift, if its absolute magnitude were equal to $M_r^{lim} = -19.8$. This can be achieved by converting the mass-to-light ratio fitted by BMA through $\mathrm{Log}(M_\star^{lim}) = \mathrm{Log}(M_\star) + 0.4(M_r - M_r^{lim})$, where M_r and $M_\star$ are the galaxy estimated absolute magnitude and stellar mass. From Figure 2 it is clear that, if all the galaxies were at M_r^{lim} or fainter, $\gtrsim 90\%$ of them would have a stellar mass $\lesssim 10^{10} M_\odot$. We therefore are $\gtrsim 90\%$ complete above $M_\star = 10^{10} M_\odot$ over the whole redshift range. The scatter in mass at each redshift is given by the scatter in M/L of the different models. We therefore cut our stellar mass sample at $M_\star > 10^{10} M_\odot$.

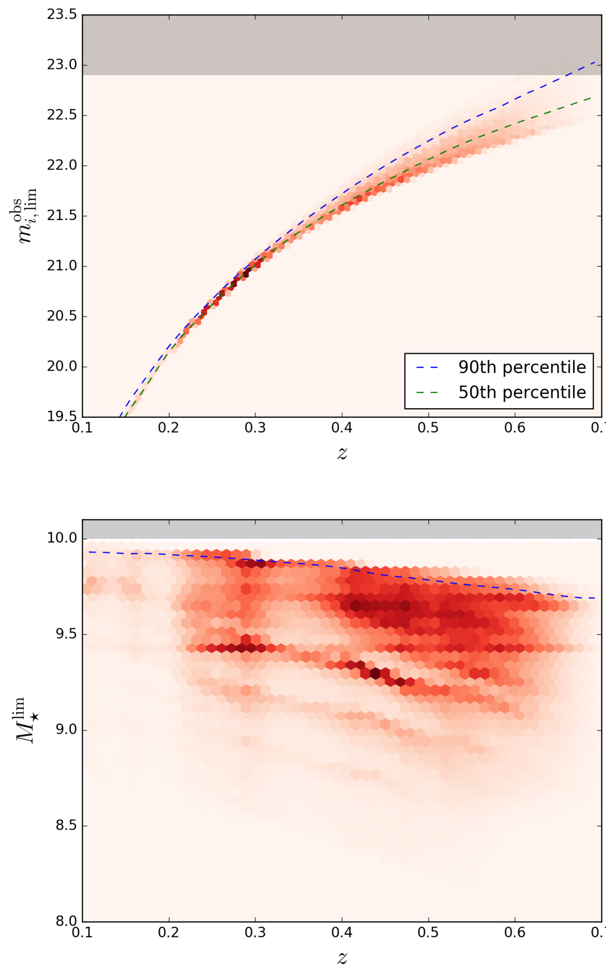

Figure 2. Analysis of the completeness of the galaxy sample. *Top panel:* observed i-band magnitudes that the galaxies in our sample would have if they had the absolute magnitude used as our limit ($M_r^{\rm lim} = -19.8$). The shadowed region represents the DES Y1 95% completeness limit from Drlica-Wagner et al. (2018). *Bottom panel:* limiting mass $M_\star^{lim}$ that each galaxy would have, at its redshift, if its absolute magnitude were equal to $M_r^{lim} = -19.8$. The limiting mass is below $10^{10} M_\odot$ at all redshifts; we therefore cut our sample at this stellar mass. The shadowed region represents this cut. The dashed lines are the 50th and 90th percentile of the distributions.

2.2 X–ray catalogues

The $\mu_\star$–X–ray mass observable relations are computed using archival *XMM* and *Chandra* data. The DES Y1 redMaPPer cluster catalogue is used to find galaxy clusters in the X–ray databases at the same positions. Consequently, the samples are not X–ray selected. However, X–ray temperature and luminosity measurements are not available for all of the redMaPPer clusters, either due to a lack of archival observation, or the number of photons are not enough to estimate the luminosity or temperature.

The X–ray Multi–Mirror Mission (*XMM*; Jansen & Laine 1997) is a European Space Agency space mission launched in 1999. The *XMM* Cluster Survey (*XCS*) consists in a search for galaxy clusters in archival *XMM-Newton* observations. In order to derive the cluster X–ray temperature and luminosity, we use the *XCS* Post Processing Pipeline (`XCS3P`) as described in Giles et al. (in prep), and briefly describe the methodology here. Cluster spectra are extracted and fitted using the XSPEC (Arnaud 1996) package, performed in the 0.3-7.9 keV band with an absorbed MeKaL model. The cluster spectra are extracted within r_{2500c}, which is estimated through an iterative procedure. An initial temperature is estimated using the XAPA source detection region (Lloyd-Davies et al. 2011), and r_{2500c} estimated from the r_{2500c}-kT relation of Arnaud, Pointecouteau & Pratt (2005). This process is then iterated until r_{2500c} converged to within 10%. Furthermore, a calculation of coefficient of variation (Koopmans, Owen & Rosenblatt 1964) of T_X is performed, defined as the ratio of the standard deviation (σ) to the mean (μ), given by $C_v = \sigma(T_X)/\mu(T_X)$. In this work, we adopt a value of $C_v < 0.25$ as an indicator of a reliable measurement of the iterative temperature. Furthermore, luminosities in this work are calculated in the 0.5–2.0 keV band (cluster rest frame). The final sample is composed of 80 clusters in the DES Y1 wide field.

The *Chandra X–ray Observatory* is a NASA telescope launched in 1999. In order to obtain X–ray temperatures and luminosities for archival *Chandra* data, we use the Mass Analysis Tool for *Chandra* (`MATCha`) pipeline, described in Hollowood et al. (2018). This pipeline finds, downloads, and cleans archival *Chandra* data for each of its input cluster candidates. It then iteratively finds a galaxy cluster center (until converged within 15 kpc), and iteratively fits X–ray temperatures and luminosities within 500 kiloparsec, r_{2500c}, and r_{500c} apertures (until converged within 1σ). As with `XCS3P`, `MATCha` performs its fitting using XSPEC, with an absorbed MeKaL model. As in `XCS3P`, `MATCha` performs its fits within the 0.3–7.9 keV band. For consistency with the *XCS* selection, we apply the same SNR cut to this sample. We choose to use temperatures within r_{2500c} for this sample because they are more accurate for nearby clusters, where the the r_{500c} apertures becomes too big compared to the *Chandra* chip. Matching again the *XMM* analysis above, luminosities are estimated in the 0.5–2.0 keV band. Our final *Chandra* sample is composed of 70 clusters in the DES Y1 wide field.

In order to perform a joint fit between the two X–ray samples and improve our population statistics, we correct for a systematic misalignment between the *Chandra* and *XMM* temperature measurements, as estimated by Rykoff et al. (2014):

$$\mathrm{Log}(T_X^{\mathrm{Chandra}}) = 1.0133\mathrm{Log}(T_X^{\mathrm{XMM}}) + 0.1008\,, \qquad (1)$$

where the temperatures are in keV. In the following, we use eq. (1) to convert *XMM* temperatures.

3 METHOD

3.1 Stellar mass estimation

3.1.1 Stellar mass with Bayesian Model Averaging

A major cause of uncertainty in stellar mass estimation from broadband photometry is in the model assumptions (see e.g. Mitchell et al. 2013) that are needed in model fitting techniques. These assumptions mainly involve redshift, star formation history (SFH), the initial mass function (IMF), the dust content and the knowledge of stellar evolution at all stages. Rykoff et al. (2016) showed that the redMaPPer photometric redshifts for DES are excellent, with errors of the order $\sigma_z/(1+z) \sim 0.01$ up to $z \sim 0.9$. This allows us to safely assume the cluster redshift for the cluster members and to avoid exploring the photo–z dependence of stellar masses, as was done in another DES study by Capozzi et al. (2017). Despite the fact that in the present work we can safely assume that the cluster redshift is a good estimate of the real galaxy redshift, all the other assumptions remain unconstrained. We therefore choose not to ignore the uncertainty on model selection and use a set of robust, up-to-date stellar population synthesis (SPS) models and average over all of them, marginalizing over the model uncertainty. The method used here is called Bayesian Model Averaging (BMA, see e.g. Hoeting et al. 1999). BMA has already been successfully applied to galaxy SED fitting parameter estimation in Taylor et al. (2011).

Our code can be used to estimate physical parameters of galaxies (stellar masses, specific star formation rates, ages, metallicities) as well as cluster stellar masses and total star formation rate (SFR) when provided with cluster membership probabilities, and it is publicly available at `https://github.com/apalmese/BMAStellarMasses`.

The BMA starting point is Bayes' theorem, through which we can write the posterior probability distribution $p(\bar{\theta}_k|D, M)$ of the set of parameters $\bar{\theta}_k$ given the data D and the model M_k:

$$p(\bar{\theta}_k|D, M_k) = \frac{p(D|M_k, \bar{\theta}_k)p(\bar{\theta}_k|M_k)}{p(D|M_k)}\,, \qquad (2)$$

where $p(D|M_k, \bar{\theta}_k)$ is the likelihood, $p(\bar{\theta}_k|M_k)$ is the prior probability of the parameters given the model M_k, and $p(D|M_k)$ is the evidence. In our case, the set of parameters $\bar{\theta}_k$ define the stellar population properties (e.g. stellar mass, SFH parameters, metallicity) of model M_k, and the data D are the galaxy's observed magnitudes.

The model averaged posterior distribution of the parameters θ_k is given by the sum of the single model M_k posteriors, weighted by the model prior:

$$p(\bar{\theta}_k|D) = \frac{\sum_k p(\bar{\theta}_k|D, M_k)p(M_k)}{\sum_k p(M_k|D)}\,. \qquad (3)$$

From BMA it also follows that the posterior distribution of a quantity Δ is the average of the single model posteriors for that quantity, weighted by their posterior model probability:

$$p(\Delta|D) = \sum_k p(\Delta|D, M_k)p(M_k|D)\,. \qquad (4)$$

The posterior model probabilities can be computed by:

$$p(M_k|D) = \frac{p(D|M_k)p(M_k)}{\sum_k p(D|M_k)p(M_k)}\,, \qquad (5)$$

where

$$p(D|M_k) = \int p(D|M_k, \bar{\theta}_k)p(\bar{\theta}_k|M_k)\mathrm{d}\bar{\theta}_k\,. \qquad (6)$$

In our case $p(\bar{\theta}_k|M_k)$ is simply a delta function, as the parameters $\bar{\theta}_k$ (i.e. the SFH parameters, metallicities, etc.) fully define our models M_k.

From Eq. (6) one can write:

$$\langle\Delta\rangle = \sum_k \bar{\Delta}_k p(M_k)\mathcal{L}_k\,, \qquad (7)$$

where $\bar{\Delta}_k$ is the mean Δ value from the model M_k, which is defined by the set of parameters $\bar{\theta}_k$ including metallicity and SFH parameters. $\mathcal{L}_k$ is the likelihood $p(D|M_k)$ that we will reconstruct from the χ^2 distribution. The model prior $p(M_k)$ is uniform over all models.

In our code, the mass-to-light ratio $M_\star/L$ is the quantity Δ. Its posterior mean over all the models considered is then used to estimate the stellar mass $M_\star$ of each single galaxy through:

$$\mathrm{Log}(M_\star/M_\odot) = \langle M_\star/L\rangle - 0.4(i - DM + \langle kii\rangle - 4.58)\,, \qquad (8)$$

where $\langle M_\star/L\rangle$ is the weighted mean stellar-mass-to-light-ratio in solar mass units, i is the observed i band magnitude,

Parameter	Values
Z	0.03, 0.019, 0.0096, 0.0031
t_i [Gyr]	0.7, 1.0, 1.5, 2.0
t_t [Gyr]	7, 9, 11, 13
τ [Gyr]	0.3, 1.0, 1.3, 2.0, 9.0, 13.0
θ [deg]	−10, −20, −30, −40, −50, −80

Table 1. Parameters of the models used in the BMA SED fitting.

DM is the distance modulus, $\langle kii \rangle$ is the weighted mean of the K-correction $i_{\rm restframe} - i$ and 4.58 is the i-band absolute magnitude of the Sun. Weighted means are considered over all models.

In this work we use the flexible stellar population synthesis (FSPS) code by Conroy & Gunn (2010) to generate simple stellar population spectra. Those are computed assuming Padova (Girardi et al. 2000, Marigo & Girardi 2007, Marigo et al. 2008) isochrones and Miles (Sánchez-Blázquez et al. 2006) stellar libraries with four different metallicities ($Z = 0.03, 0.019, 0.0096$ and 0.0031). We choose the four-parameter SFH described in Simha et al. (2014):

$$SFR(t) = \begin{cases} A(t - t_i)\mathrm{e}^{(t-t_i)/\tau} & \text{if } t < t_t \\ SFR(t_t) + \Gamma(t - t_t) & \text{otherwise} \end{cases} \tag{9}$$

where t_i is the time at which star formation commences ($\sim$ 1 Gyr), t_t is the time when the SFR transitions from exponential to a linear fall off ($\sim$ 9 Gyr), τ is the exponential time scale, and Γ is the slope of the linearly decreasing SFR as a function of time t after t_t. Defining θ as $\Gamma \equiv \tan\theta$, we make the four parameters vary on a grid of values within the following ranges: $\tau \in [0.3, 13]$ Gyr, $t_i \in [0.7, 2]$ Gyr, $t_t \in [7, 13]$ Gyr, and $\theta \in [-10, -80]$ deg. Table 1 reports the grid of values used for these parameters.

For each observed galaxy we construct the likelihood $\mathcal{L}_k$ in Eq. (7) as $\mathcal{L}_k \propto e^{-\chi^2_k/2}$, with:

$$\chi^2_k = \sum_j \frac{(C_i - C_{k,j})^2}{\sigma^2_{C_j}}\,, \tag{10}$$

where the sum is over the colours $g-r$, $r-i$, and $i-z$. C_j are the observed colours, while $C_{k,j}$ are the colours predicted by the model M_k for the colour j. The scaling for the theoretical model is given by the i band filter. σ_{C_j} are the observed errors added in quadrature with a lower limit of 0.02.

3.1.2 Validation of the BMA method

In order to test our method for stellar mass estimation, we use as reference a catalog that overlaps with DES observations. Laigle et al. (2016) used LePhare to compute stellar masses with multiband data in 16 filters from UV to infrared over the 2 deg^2 COSMOS field. From this sample, matched to DES data, we remove all objects at $z = 0$ to eliminate stars, and at $z > 1.5$, as higher redshift galaxies are beyond the interests of this work. Galaxies with i-band magnitude above 23.0 are also cut out. The remaining sample comprises galaxies with $SNR > 10$ in DES, for which we compute stellar masses using the BMA code and DES data. The bias distribution given by the difference in log galaxy stellar mass between the two samples $\mathrm{Log}(M_\star^{\rm COSMOS}) - \mathrm{Log}(M_\star^{\rm BMA})$ is shown in Figure 3. Mean bias and scatter (that we quantify as the standard deviation of the distribution) are below the typical error on galaxy stellar masses from SED fitting ($\sim$ 0.2 dex) in the redshift range $0.2 < z < 0.6$, where we expect good performance for optical surveys such as DES. At higher redshift, it is harder to constrain the optical to near-infrared (NIR) SED with the DES bands and therefore the scatter increases. Also at low redshifts ($z < 0.2$), the 4000Å break is harder to constrain, as it is blue-ward of the g-band effective wavelength. The slight bias that seems to exist in our DES stellar masses, particularly towards higher redshift, is probably due to the degeneracies between stellar

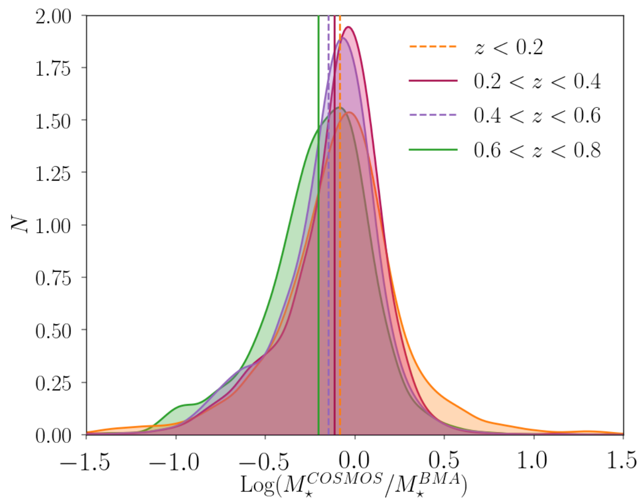

Figure 3. Comparison of galaxy stellar masses from Laigle et al. (2016) using COSMOS data with those computed with the BMA algorithm using DES data in different redshift bins. The lines represent the mean value of the distributions with the same colour. The histograms have been smoothed with a Gaussian kernel for visualization purposes, and arbitrarily renormalised. The total number of galaxies used is $\sim 120,000$.

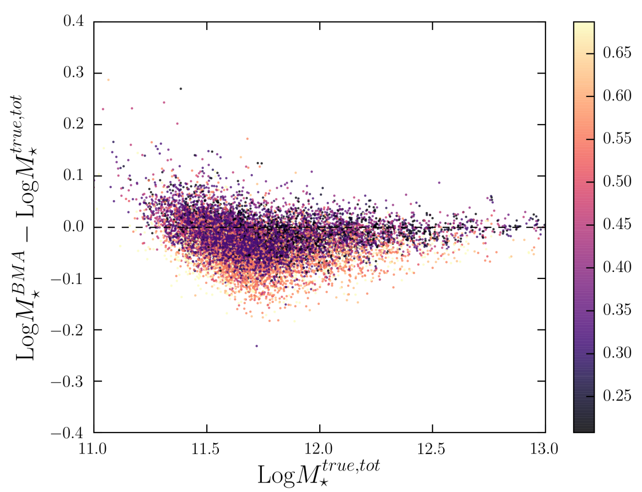

Figure 4. Comparison of BMA clusters stellar mass to Millennium simulation true values at different redshifts. The dashed lines indicates no difference between the BMA estimates and the true values.

mass and dust extinction. Laigle et al. (2016) are able to constrain dust extinction better than in this work because of the information brought by the infrared data available to them. Overall, differences between the two catalogues will also be partially due to the fact that the COSMOS stellar masses are not "true" stellar masses, and will depend on the assumptions and methodology in Laigle et al. (2016). Among those assumptions, the synthetic templates assumed by Laigle et al. (2016) are from Bruzual & Charlot (2003), and thus will differ from the models assumed here.

We also test our results against the Millennium simulation semi–analytic model from De Lucia & Blaizot (2007)[5], and show the results for the sum of stellar mass in clusters (selected as halos with $M_{200c} > 10^{14}\ M_{\odot}$), in Figure 4. We run the BMA algorithm using the simulated magnitudes for the *griz* SDSS filters, which are very similar to the DES ones. In this case the scatter of the bias distribution is even lower (standard deviation is ~ 0.04 dex) than what found in the comparison with the COSMOS results, showing that our method works well against other SED fitting methods and simulations.

3.2 From galaxy stellar masses to $\mu_\star$

The cluster mass proxy $\mu_\star$ is computed by weighing the stellar mass of each galaxy in the cluster by its membership probability $p_{\mathrm{mem},i}$:

$$\mu_\star = 10^{-10} M_\odot^{-1} \sum_i p_{\mathrm{m},i} M_{\star,i}\,, \tag{11}$$

where the factor 10^{-10} simply gives to the mass proxy an order of magnitude similar to that of the number of observed cluster galaxies. The sum is over all the galaxies from the DES Y1A1 gold catalog having $M_r < -19.8$ and within 3 Mpc from the centre of the cluster as given by the redMaPPer Y1 catalog. The membership probability is computed as described in Welch et al. (2019), where the membership assignment scheme is presented in detail, together with measurements of the red sequence for redMaPPer clusters. The probability is given by

$$p_{\mathrm{m}} = p_R\, p_z\,, \tag{12}$$

where the components represent the probability of the galaxy being a member given its redshift (p_z) and its distance from the cluster center (p_R). The radial probability p_R is assigned by assuming a projected Navarro–Frenk–White (NFW; Navarro, Frenk & White 1996) profile, with R_{200c} computed by counting galaxies within 3 Mpc and finding the halo profile by assuming an HOD model. The redshift probability p_z is computed by comparing the photo–z $p(z)$ of single galaxies to the cluster redshift. The membership probability presented here differs from the one provided by redMaPPer because it uses photometric redshift information, instead of a red sequence calibration. The computation of the radial probability is similar, as it assumes the same function for the galaxy profile, while the radius may be different as our method utilises the HOD model.

We also provide a colour probability p_{c} estimated through a Gaussian Mixture Model (GMM) similar to Hao et al. (2009). This method fits two Gaussians to the colour distribution of the galaxies in each cluster, weighted by their radial and redshift probabilities. The Gaussians fit the colour distribution of the red sequence and blue cloud of cluster galaxies well. The area of the Gaussians w_{red} and w_{blue} satisfies $w_{\mathrm{red}} + w_{\mathrm{blue}} = 1$ and is used to compute the colour probability:

$$p_{\mathrm{c}} = w_{\mathrm{red}} p_{\mathrm{red}} + w_{\mathrm{blue}} p_{\mathrm{blue}}\,, \tag{13}$$

where p_{red} (p_{blue}) is the probability that a galaxy belongs to the red sequence (blue cloud) given its colour and the GMM estimates. The cluster colour distribution is derived after a local background subtraction is performed by measuring the colour distribution of galaxies in the cluster outskirts (between 3 and 5 Mpc). This is done for the colours $g-r$, $r-i$, and $i-z$. The inclusion of the colour term is tested in Section 4. See Welch et al. (2019) for a full description of the membership probability scheme.

The errors on $\mu_\star$ were computed using jackknife resampling. Intuitively, this method allows us to estimate the variance on our estimator by considering a galaxy cut from the cluster at each time.

3.3 Hot gas temperature – stellar mass relations

Following previous works (e.g. Rozo et al. 2009a; Rozo et al. 2011; Evrard et al. 2014; Mulroy et al. 2019; Farahi et al. 2019), we assume that the likelihood of a cluster to have X–ray temperature T, given that it has a stellar mass $\mu_\star$, is a log-normal function. Following the notation in Evrard et al. (2014) and Farahi et al. (2019):

$$P(T|\mu_\star, z) = \frac{1}{\sqrt{2\pi}\sigma_{\ln T|\mu_\star}} \exp\Big[-\frac{(\ln T - \langle \ln T|\mu_\star, z\rangle)^2}{2\sigma^2_{\ln T|\mu_\star}}\Big]\,, \tag{14}$$

where $\sigma_{\ln T|\mu_\star}$ is the intrinsic scatter of the hot gas temperature at fixed stellar mass, $\mu_\star$. We perform a Bayesian linear regression (Kelly 2007) to estimate a linear relation between the logarithm of the X–ray temperature and the logarithm of stellar mass. The free parameters include normalization, slope, and the scatter about the mean relation. Namely, we fit:

$$\langle \ln T|\mu_\star, z\rangle = \big[\pi_{T|\mu_\star} + \frac{2}{3}\ln(E(z))\big] + \alpha_{T|\mu_\star} \ln\Big(\frac{\mu_\star}{\tilde{\mu}_\star}\Big)\,, \tag{15}$$

where $\tilde{\mu}_\star$ is the median $\mu_\star$ of the sample and $E(z) = H(z)/H_0$ is the Hubble parameter evolution. The normalization term containing $E(z)$ takes into account the redshift dependence of the temperature, as expected for a self–similar evolution of the intra-cluster medium in virial equilibrium (Kaiser 1991; Bryan & Norman 1998). We use the publicly available Python version of Kelly (2007) to perform this regression, which provides samples from the posterior distribution of the normalization, $\pi_{T|\mu_\star}$, slope, $\alpha_{T|\mu_\star}$, and scatter about the mean relation, $\sigma_{\ln T|\mu_\star}$.

3.4 Mass scatter inference

We follow Evrard et al. (2014) and Farahi et al. (2019) model to infer the halo mass scatter at fixed $\mu_\star$. Evrard et al. (2014) proposed a population model which computes a closed form

[5] `http://gavo.mpa-garching.mpg.de/Millennium/Help?page=databases/millimil/delucia2006a`

solution for conditional properties of an observable, here T_X, given a selection observable, here stellar mass $\mu_\star$, as a function of their halo properties. We employ their model to infer the halo mass scatter. In the following, we denote the log of halo mass by $\ln M$. According to their population model, the scatter in temperature at fixed $\mu_\star$ can be written as:

$$\frac{\sigma^2_{\ln T|\mu_\star}}{\alpha^2_{T|M}} = \left[\sigma^2_{\ln M|\mu_\star} + \sigma^2_{\ln M|T} - 2r_{\mu_\star T}\sigma_{\ln M|\mu_\star}\sigma_{\ln M|T}\right]. \tag{16}$$

We employ $\sigma_{\ln M|T} = \sigma_{T|\ln M}/\alpha^2_{T|M}$ and solve for $\sigma_{\ln M|\mu_\star}$, which is the quantity of interest. After rearrangement, the solution yields

$$\sigma^2_{\ln M|\mu_\star} = \sigma^2_{\ln M|T}\left[\left(\frac{\sigma^2_{\ln T|\mu_\star}}{\sigma^2_{\ln T|M}} - (1 - r^2_{\mu_\star T})\right)^{1/2} + r^2_{\mu_\star T}\right]^2, \tag{17}$$

where $r_{\mu_\star T}$ is the correlation coefficient between $\mu_\star$ and temperature deviations about their mean values at fixed halo mass.

4 RESULTS AND DISCUSSION

4.1 X–ray scaling relations

We first separately fit the X–ray temperatures presented in Section 2.2 for the *XMM* and *Chandra* samples. The results of the regression are reported in Table 2 and shown in Figure 5. A few outliers are clearly visible in both samples, particularly in the low–T_X regime. Only one data point (shown in lighter grey in Figure 5) has a significant deviation from the mean relation ($> 3\sigma_{\ln T/L_X|\mu_\star}$), and it has been excluded from the regression. These outliers tend to have a higher $\mu_\star$ than expected from the mean scaling relation. It is likely that these estimates are affected by the presence of structure along the line of sight, which boosts the mass proxy value. A similar behaviour is also found in Farahi et al. (2019) for the same clusters for the redMaPPer richness, which is computed through a very different methodology, meaning that the outliers are likely related to the galaxies in the DES catalogue rather than to the method.

We have tested the dependence of the scaling relation results on the completeness of the cluster catalogue. In fact, the X–ray catalogue is likely to be incomplete at the low–temperature end. Farahi et al. (2019) find that the X–ray matched redMaPPer catalogue is ~ 50 per cent complete at $\lambda \sim 100$. This corresponds to $\mu_\star \sim 1000$ based on the stellar mass–richness relation found in Palmese et al. (2019). We find that, cutting our cluster sample at $\mu_\star > \mu_\star^{\rm cut} = 1000$ or higher values, provides scaling relation constraints which are less stringent than those reported in Table 2, but still consistent within 1σ.

The weak lensing mass–$\mu_\star$ relation studied in Pereira et al. (2018) shows a steeper slope (1.74 ± 0.62 at $0.1 < z < 0.33$ for SDSS redMaPPer clusters) than the analysis presented here. We believe that the correlation of stellar mass with total cluster mass is higher than with the X–ray temperatures because the X–ray measurement only probes the inner part of the cluster gravitational potential (within R_{500c} and R_{2500c} for the *XMM* and *Chandra* data respectively), while the weak lensing probes larger radii, thus correlating better with the total stellar mass content.

We perform the same linear regression of Eq. (15) with the X–ray luminosities in units of 10^{44}erg/s in place of the temperatures. Results are reported in Table 2. We find a larger scatter for this relation, which is expected as the temperature directly probes the potential well of the halo, while the luminosity depends primarily on the density of the Intra–cluster Medium (ICM). This causes baryon effects to be included to a higher order and the scatter with halo mass to increase.

4.2 Intrinsic temperature scatter

We find an intrinsic scatter in temperature at fixed $\mu_\star$ of $\sigma_{\ln T_X|\mu_\star} = 0.277^{+0.026}_{-0.029}$ for the *XCS* sample. This value is below the value found for the redMaPPer optical–richness (0.289 ± 0.025) in Farahi et al. (2019), although by less than 1σ significance level.[6] The scatter on ln T_X from the *Chandra* sample is even lower ($0.229^{+0.025}_{-0.027}$) and it is $\sim 1\sigma$ below the redMaPPer richness estimate (0.260 ± 0.032). The joint scatter for the two samples is $0.266^{+0.019}_{-0.020}$. The values found for the intrinsic scatter are comparable to what is found for λ, and as such they are promising. The redMaPPer richness is an optimized *count* observable, and the stellar mass observable has a consistent scatter. We expect $\mu_\star$ to be affected by projection effects similarly to λ (as described in Costanzi et al. 2019) or somewhat worse (if the photo–z's do not perform well). It should thus have similar or smaller scatter on the basis of individual halos than is possible from counts alone.

We perform a number of tests to understand if the membership probabilities are taken into account in an optimal way. We find that including the blue cloud galaxies does not bring a significant increase in the scatter: the inclusion of the second term in the right-hand side of Eq. (13), compared to having solely the red sequence term or redMaPPer members, brings an additional scatter which is an order of magnitude lower than the error. This is consistent with what we would expect for this sample, as it has been matched to a red-sequence cluster finder. Rozo et al. (2011) found that the blue galaxies significantly increase the scatter of their sample, but the fact that this is not true in our case allows us to keep this contribution which may become relevant at low richness and high redshift regimes, which should be tested using a non-red sequence based cluster finder and matched against other mass observables. It is beyond the scope of this work to test this hypothesis. Rozo et al. (2011) also show that differences between the true and predicted scatter of the mass proxy–mass relation are irrelevant for a DES-like survey as long as these differences are about 5% or less (i.e., $\Delta\sigma < 0.05$), which further supports our choice.

We find that the inclusion of the radial probability works well in terms of the choice of an arbitrary radial cut between 0.7 and $3h^{-1}$ Mpc: In fact, the intrinsic scatter of the temperature-mass relation is independent of this choice. On the other hand, we tested the use of the red galaxies only without including the radial probability contribution.

[6] σ here refers to the error on the scatter.

Sample–observable	$\pi_{\ln T/L_X\|\mu_\star}$	$\alpha_{\ln T/L_X\|\mu_\star}$	$\sigma_{\ln T/L_X\|\mu_\star}$	$\ln(\tilde{\mu}_\star)$
XMM–T_X	$1.306^{+0.035}_{-0.035}$	$0.449^{+0.054}_{-0.055}$	$0.277^{+0.026}_{-0.029}$	6.61
Chandra–T_X	$1.887^{+0.032}_{-0.032}$	$0.463^{+0.072}_{-0.072}$	$0.229^{+0.025}_{-0.027}$	7.07
Chandra+XMM–T_X	$1.711^{+0.024}_{-0.025}$	$0.488^{+0.043}_{-0.043}$	$0.266^{+0.019}_{-0.020}$	6.85
Chandra+XMM–T_X $(z < 0.3)$	$1.781^{+0.041}_{-0.042}$	$0.501^{+0.084}_{-0.084}$	$0.262^{+0.029}_{-0.033}$	6.79
Chandra+XMM–T_X $(0.3 < z < 0.5)$	$1.753^{+0.035}_{-0.036}$	$0.497^{+0.056}_{-0.055}$	$0.263^{+0.027}_{-0.031}$	7.03
Chandra+XMM–T_X $(z > 0.5)$	$1.682^{+0.066}_{-0.065}$	$0.54^{+0.13}_{-0.14}$	$0.311^{+0.051}_{-0.064}$	6.91
XMM–L_X	$1.11^{+0.11}_{-0.11}$	$1.61^{+0.18}_{-0.18}$	$0.963^{+0.078}_{-0.087}$	6.61
Chandra–L_X	$1.77^{+0.10}_{-0.10}$	$1.22^{+0.23}_{-0.23}$	$0.813^{+0.075}_{-0.084}$	7.07

Table 2. Scaling relation parameters from this work following Eq.(15) for X–ray temperatures and luminosities. The upper part of the table shows our results for the temperature over the whole $0.1 < z < 0.7$ redshift range. The middle section presents results in different redshift bins for the temperatures from the joint *Chandra+XMM* sample. The bottom part reports results for the luminosities. Values represent the median of the parameters posterior distribution, and the errors are the 16th and 84th percentiles. Temperatures are in units of keV and luminosities in $10^{44}\mathrm{erg s}^{-1}$

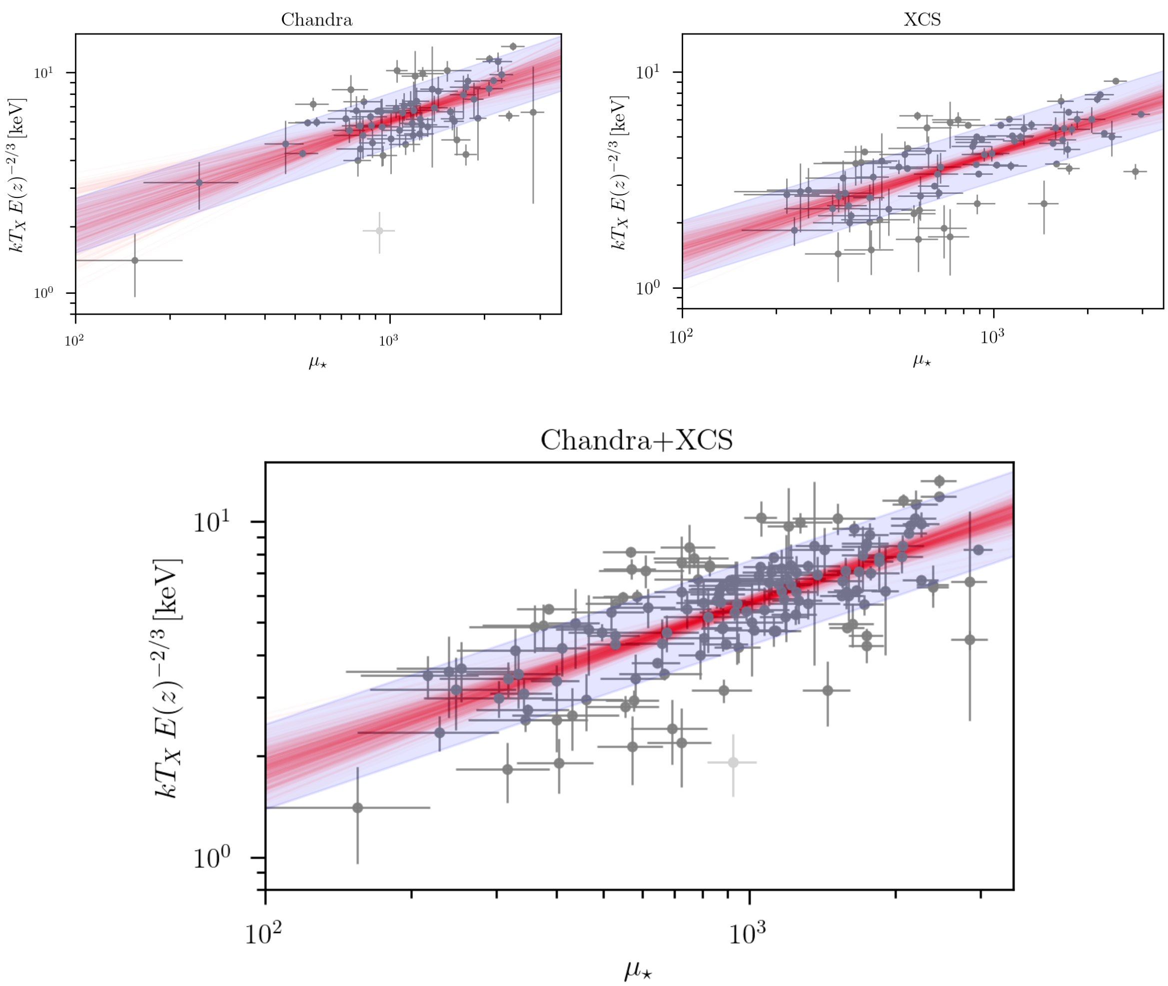

Figure 5. Bayesian linear regression of *X*-ray temperature and $\mu_\star$ for the *Chandra* and XMM samples (top panels) and for the joint sample (bottom panel). The red lines are a random sample from the posterior distribution of slope and intercept, and the blue band represents 1σ around the mean value of the intercept plus the intrinsic scatter. The light grey point has been excluded from the regression because it is an outlier with significant deviation from the mean relation ($> 3\sigma_{\ln T/L_X|\mu_\star}$).

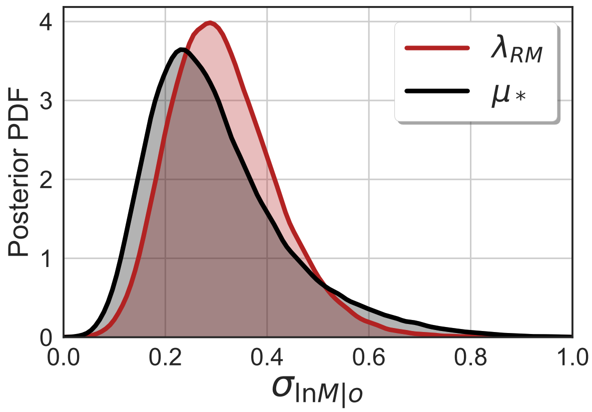

Figure 6. Posterior distribution of the scatter in total mass at fixed mass observable o ($\mu_\star$ in black and λ in red) for the joint cluster sample. In this work we find: $\sigma_{\ln M|\mu_\star} = 0.26^{+0.15}_{-0.10}$.

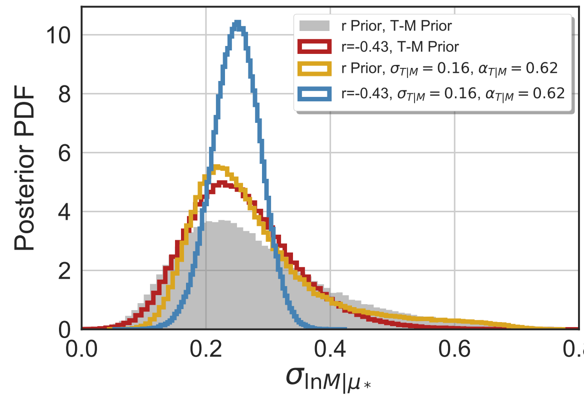

Figure 7. Posterior distribution of the scatter in total mass at fixed $\mu_\star$ for the joint cluster sample, showing the impact of different uncertainties on the final PDF. The grey region corresponds to the grey PDF in Figure 6. The other lines show the same pdf, when some of the parameters in the right–hand–side of Eq. (17) are fixed to a known value, and the others are allowed to vary. The red line assumes that the correlation coefficient is fixed at $r_{\mu_\star T} = -0.43$, while the yellow line is computed by fixing the slope and scatter in the $T - M$ relation. The blue line fixes all those quantities, except for the $T - \mu_\star$ scatter derived in this work.

In this case, we find similar trends to previous work (e.g. Andreon 2015): Optimal choices for the aperture *do* exist when no membership probability is considered. We find that the scatter can increase by up to $\sim 15\%$ within the inner 1.5 Mpc, and outside that range mostly noise is added.

We tested the inclusion of colour probabilities p_c in the full membership probabilities by modifying Eq. (12) into $p_{\rm m} = p_R p_z p_c$. We also tried to combine the colour membership probabilities from different colours in different redshift ranges. This is justified by the fact that most of the colour information in a galaxy SED is contained in the 4000 Å break, that shifts between the bands with redshift. We therefore use $g - r$ for the range $z < 0.35$, $r - i$ in $0.35 < z < 0.75$ and $i - z$ at $z > 0.75$. We find that these tests did not have a significant impact on the mean scaling relation fit and intrinsic scatter, so it is reasonable to include the simpler version of the full probabilities as given in Eq. (12).

The fact that our scaling relation scatter and slope are insensitive to the choices made in these tests shows that the membership probabilities are robust and that cluster size and colours (that enter in $p_{\rm m}$ through the redshift probability estimation) are taken into account well.

In order to test the redshift dependence of the scaling relation, we split the joint cluster sample into three subsamples ($z < 0.3$, $0.3 < z < 0.5$ and $z > 0.5$) and perform the same linear regression presented above over the whole redshift range. Slope, intercept and scatter are all consistent over the different redshift bins. We conclude that we find no evidence for a redshift evolution of the scaling relation out to $z < 0.7$. We believe that this result is related to the fact that the stellar mass content of galaxy clusters is mostly formed before redshift ~ 1, and it is consistent with other results (e.g. Chiu et al. 2018) and simulations (Farahi et al. 2018).

4.3 Total mass scatter

In order to estimate the scatter in mass at fixed $\mu_\star$ presented in Eq. (17) we need to have an estimation of the correlation coefficient $r_{\mu_\star T}$, the scatter in temperature at fixed total mass and the scatter in mass at fixed temperature. The correlation coefficient of pairs of nine observables is estimated by Farahi et al. (in prep.) by employing multi-wavelength analysis of 41 X–ray selected cluster from the LoCuSS clusters sample (Mulroy et al. 2019). We employ their L_K–T_X correlation coefficient which serves as a good approximation of the stellar mass–temperature correlation in our sample. Their posterior estimate of the correlation coefficient is $r_{\mu_\star T} = -0.43^{+0.49}_{-0.35}$. The additional parameters needed in Eq. (17), namely $\sigma_{\ln T|M}$ and $\sigma_{\ln M|T}$, are taken from the recent constraints on the scaling relation between the temperature and total mass from weak lensing for the Weighing the Giants program (Mantz et al. 2015, 2016). Their posterior constraints read $\sigma_{\ln T|M} = 0.16 \pm 0.02$ and $\alpha_{T|M} = 0.62 \pm 0.4$. We employ $\sigma_{\ln M|T} = \sigma_{\ln T|M}/\alpha_{T|M}$ to get an estimate of mass scatter at fixed X–ray temperature. The posterior distribution of $\sigma_{\ln M|\mu_\star}$ is then obtained by Monte Carlo sampling the right-hand-side of Eq. (17).

Parameter	Value	Sample
$\sigma_{\ln T\vert M}$	0.16 ± 0.02	Weighing the Giants
$\alpha_{T\vert M}$	0.62 ± 0.04	Weighing the Giants
$r_{\mu_\star T}$	$-0.43^{+0.49}_{-0.35}$	LoCuSS
$\sigma_{\ln M\vert\mu_\star}$	$0.19^{+0.15}_{-0.09}$	*Chandra*
$\sigma_{\ln M\vert\mu_\star}$	$0.28^{+0.16}_{-0.11}$	*XMM*
$\sigma_{\ln M\vert\mu_\star}$	$0.26^{+0.15}_{-0.10}$	*Chandra+XMM*

Table 3. Parameters used to estimate the mass scatter in Eq. (17) (upper part of the table), and results from this work (lower table).

The result for the joint X–ray sample is shown in Fig. 6. For the *Chandra* and *XMM* samples we find $\sigma_{\mu|\mu_\star} = 0.19^{+0.15}_{-0.09}$ and $0.28^{+0.16}_{-0.11}$ respectively, while from the joint analysis $\sigma_{\mu|\mu_\star} = 0.26^{+0.15}_{-0.10}$. A summary of the parameters used and of these results is reported in Table 3. The errors on the scatter are dominated by the uncertainty on the external parameters described above. In fact, Figure 7 shows that the marginalization over the temperature–mass relation (red line) and over the correlation coefficient (yellow line) have a very similar impact on the final posterior estimate, and they dominate the final uncertainty compared to a marginalization over $\sigma_{\ln T|\mu_\star}$ only.

The scatter found here is consistent with what Farahi et al. (2019) finds for the redMaPPer richness. The slight difference is mostly driven by the lower scatter in temperature at fixed $\mu_\star$ described in Section 4.2 for the *Chandra* sample. We believe that there is room for further improvement through a more precise estimation of the correlation coefficient, which is driving the more extended tail in Figure 6 for $\mu_\star$ compared to the richness case.

Remarkably, the scatter found in this work is also consistent with what Farahi et al. (2018) find using BAHAMAS and MACSIS simulations, and a similar approach based on Evrard et al. (2014). We assume that $\mu_\star$ probes well the stellar mass content of clusters from BAHAMAS and MACSIS. For the cluster mass probed here ($M_{200c} \sim 10^{14} M_\odot$) we can derive the stellar–mass–conditioned scatter in total mass from their results through: $\sigma_{\mu|\mu_\star} \simeq \sigma_{\mu_\star|\mu}/\alpha_{\mu_\star} \simeq 0.22$.

5 CONCLUSIONS

In this work we present a stellar–mass–based mass proxy, $\mu_\star$, and its application to DES Y1 redMaPPer clusters using DES Y3 photometry. In particular, we present a code that uses Bayesian Model Averaging to compute galaxy stellar masses and other galaxy properties. The outputs of this code, along with galaxy membership probabilities presented in a companion paper, are used to estimate our mass proxy. We match Y1 redMaPPer clusters to archival *XMM* and *Chandra* data in order to study the scaling relation of $\mu_\star$ with X–ray temperature and luminosity. Assuming that the scatter in temperature around the mean of the scaling relation at a given $\mu_\star$ is lognormal, and that the temperature scales linearly with $\mu_\star$ in lognormal space, we find that our mass proxy correlates well with the X–ray temperature, with a low intrinsic scatter. Namely, we find that the slope of the scaling relation is $\alpha_{T|\mu_\star} = 0.488^{+0.043}_{-0.043}$ and the scatter is $0.266^{+0.019}_{-0.020}$ for the joint *XMM* and *Chandra* cluster sample. This scatter is consistent with what is found in a simulation study by Farahi et al. (2018). The scaling relation parameters do not show evidence for a deviation from self–similar evolution.

Constraints on the scaling relation between the temperature and total mass from the Weighing the Giants program by Mantz et al. (2016), along with the luminosity–temperature correlation coefficient estimated by Mulroy et al. (2019) on the LoCuSS sample, are then used to derive the expected scatter on halo mass at fixed $\mu_\star$. We find $\sigma_{\ln M|\mu_\star} = 0.26^{+0.15}_{-0.10}$ for the joint *XMM* and *Chandra* sample. The large uncertainty on this parameter is driven by the marginalisation over the temperature–mass relation parameters and over the correlation coefficient. Consistent values are also found with the same analysis for the well–established redMaPPer mass proxy λ, showing that $\mu_\star$ is also a potential mass observable to be employed in cosmological analyses with cluster abundances. As such, the mass scatter constrained in this work could serve as a prior on the scatter assumed in the mass observable–mass relation in a cosmological analysis of DES Y1 redMaPPer clusters employing weak lensing measurements.

It is worth noting that using the stellar mass content of galaxy clusters as mass proxies is empirically and physically motivated, and that measurements of $\mu_\star$ also allow straightforward constraints on the stellar–to–halo connection in clusters. In other words, it allows us to better understand how galaxies evolve in clusters through estimates of their stellar content, while providing a useful tool for cosmological analyses.

Overall, our results show that $\mu_\star$ is a promising low–scatter mass proxy, which can be used as an alternative to λ, or in conjunction following the formalism by Evrard et al. (2014), for cosmological and astrophysical analyses with redMaPPer clusters. Future work will also include the development of a new version of the Voronoi–Tessellation cluster finder (Soares-Santos et al. 2011), that integrates this mass proxy into the pipeline (Burgad et al., in prep.).

ACKNOWLEDGMENTS

A. Palmese acknowledges the UCL PhD studentship and the URA Visiting scholar award. A. Farahi is supported by a McWilliams Postdoctoral Fellowship. O. Lahav acknowledges support from a European Research Council Advanced Grant FP7/291329. S. Bhargava acknowledges support from the UK Science and Technology Facilities Council via Research Training Grant ST/N504452/1. TOPCAT (Taylor 2005) has been extensively used in this work.
Funding for the DES Projects has been provided by the U.S. Department of Energy, the U.S. National Science Foundation, the Ministry of Science and Education of Spain, the Science and Technology Facilities Council of the United Kingdom, the Higher Education Funding Council for England, the National Center for Supercomputing Applications at the University of Illinois at Urbana-Champaign, the Kavli Institute of Cosmological Physics at the University of Chicago, the Center for Cosmology and Astro-Particle Physics at the Ohio State University, the Mitchell Institute for Fundamental Physics and Astronomy at Texas A&M University, Financiadora de Estudos e Projetos, Fundação Carlos Chagas Filho de Amparo à Pesquisa do Estado do Rio de Janeiro, Conselho Nacional de Desenvolvimento Científico e Tecnológico and the Ministério da Ciência, Tecnologia e Inovação, the Deutsche Forschungsgemeinschaft and the Collaborating Institutions in the Dark Energy Survey.

The Collaborating Institutions are Argonne National Laboratory, the University of California at Santa Cruz, the University of Cambridge, Centro de Investigaciones Energéticas, Medioambientales y Tecnológicas-Madrid, the University of Chicago, University College London, the DES-Brazil Consortium, the University of Edinburgh, the Eidgenössische Technische Hochschule (ETH) Zürich, Fermi National Accelerator Laboratory, the University of Illinois at Urbana-Champaign, the Institut de Ciències de l'Espai (IEEC/CSIC), the Institut de Física d'Altes Energies, Lawrence Berkeley National Laboratory, the Ludwig-Maximilians Universität München and the associated Excellence Cluster Universe, the University of Michigan, the National Optical Astronomy Observatory, the University of

Nottingham, The Ohio State University, the University of Pennsylvania, the University of Portsmouth, SLAC National Accelerator Laboratory, Stanford University, the University of Sussex, and Texas A&M University.

The DES data management system is supported by the National Science Foundation under Grant Number AST-1138766. The DES participants from Spanish institutions are partially supported by MINECO under grants AYA2012-39559, ESP2013-48274, FPA2013-47986, and Centro de Excelencia Severo Ochoa SEV-2012-0234. Research leading to these results has received funding from the European Research Council under the European Unions Seventh Framework Programme (FP7/2007-2013) including ERC grant agreements 240672, 291329, and 306478.

REFERENCES

Abbott T. M. C. et al., 2018, The Astrophysical Journal Supplement Series, 239, 18
Andreon S., 2012, A&A, 548, A83
Andreon S., 2015, A&A, 582, A100
Arnaud K. A., 1996, in Astronomical Society of the Pacific Conference Series, Vol. 101, Astronomical Data Analysis Software and Systems V, Jacoby G. H., Barnes J., eds., p. 17
Arnaud M., Pointecouteau E., Pratt G. W., 2005, Astronomy and Astrophysics, 441, 893
Benítez N., 2000, ApJ, 536, 571
Bertin E., Arnouts S., 1996, Astronomy and Astrophysics Supplement, 117, 393
Blanton M. R., Roweis S., 2007, AJ, 133, 734
Bruzual G., Charlot S., 2003, MNRAS, 344, 1000
Bryan G. L., Norman M. L., 1998, ApJ, 495, 80
Butcher H., Oemler, Jr. A., 1978, ApJ, 226, 559
Butcher H., Oemler, Jr. A., 1984, ApJ, 285, 426
Capozzi D. et al., 2017, ArXiv e-prints
Chiu I. et al., 2018, MNRAS, 478, 3072
Coleman G. D., Wu C.-C., Weedman D. W., 1980, ApJs, 43, 393
Conroy C., Gunn J. E., 2010, ApJ, 712, 833
Cool R. J. et al., 2013, ApJ, 767, 118
Costanzi M. et al., 2019, MNRAS, 482, 490
De Lucia G., Blaizot J., 2007, MNRAS, 375, 2
Desai S. et al., 2012, ApJ, 757, 83
Diehl H. T. et al., 2014, in Society of Photo-Optical Instrumentation Engineers (SPIE) Conference Series, Vol. 9149, Society of Photo-Optical Instrumentation Engineers (SPIE) Conference Series, p. 91490V
Donahue M. et al., 2002, ApJ, 569, 689
Drlica-Wagner A. et al., 2018, The Astrophysical Journal Supplement Series, 235, 33
Evrard A. E., Arnault P., Huterer D., Farahi A., 2014, MNRAS, 441, 3562
Farahi A. et al., 2019, in prep.
Farahi A., Evrard A. E., McCarthy I., Barnes D. J., Kay S. T., 2018, MNRAS, 478, 2618
Flaugher B. et al., 2015, AJ, 150, 150
Giles P. et al., 2019, in prep.
Girardi L., Bressan A., Bertelli G., Chiosi C., 2000, A&A, 141, 371
Hao J. et al., 2009, The Astrophysical Journal, 702, 745
Hao J. et al., 2010, ApJs, 191, 254
Hoeting J. A., Madigan D., Raftery A. E., Volinsky C. T., 1999, Statist. Sci., 14, 382
Hollowood D. L. et al., 2018, arXiv e-prints, arXiv:1808.06637
Hoyle B. et al., 2018, MNRAS, 478, 592
Ivezić Ž. et al., 2008, arXiv e-prints
Jansen F. A., Laine R., 1997, in Bulletin of the American Astronomical Society, Vol. 29, American Astronomical Society Meeting Abstracts, p. 1365
Kaiser N., 1991, ApJ, 383, 104
Kelly B. C., 2007, ApJ, 665, 1489
Kinney A. L., Calzetti D., Bohlin R. C., McQuade K., Storchi-Bergmann T., Schmitt H. R., 1996, ApJ, 467, 38
Koester B. P. et al., 2007, ApJ, 660, 239
Koopmans A. L. H., Owen D. B., Rosenblatt J. I., 1964, Biometrika, 51, 25
Laigle C. et al., 2016, ApJs, 224, 24
Laureijs R. et al., 2011, arXiv e-prints, arXiv:1110.3193
Lloyd-Davies E. J. et al., 2011, MNRAS, 418, 14
Mantz A. B., Allen S. W., Morris R. G., Schmidt R. W., von der Linden A., Urban O., 2015, MNRAS, 449, 199
Mantz A. B. et al., 2016, MNRAS, 463, 3582
Marigo P., Girardi L., 2007, A&A, 469, 239
Marigo P., Girardi L., Bressan A., Groenewegen M. A. T., Silva L., Granato G. L., 2008, A&A, 482, 883
Melchior P. et al., 2016, ArXiv e-prints
Miller C. J. et al., 2005, AJ, 130, 968
Mitchell P. D., Lacey C. G., Baugh C. M., Cole S., 2013, MNRAS, 435, 87
Mohr J. J. et al., 2012, Society of Photo-Optical Instrumentation Engineers (SPIE) Conference Series, 8451, 0
Mulroy S. L. et al., 2019, MNRAS
Navarro J. F., Frenk C. S., White S. D. M., 1996, ApJ, 462, 563
Oemler, Jr. A., 1974, ApJ, 194, 1
Oguri M., 2014, MNRAS, 444, 147
Palmese A. et al., 2019, in prep.
Palmese A. et al., 2016, MNRAS, 463, 1486
Pereira M. E. S. et al., 2018, MNRAS, 474, 1361
Press W. H., Schechter P., 1974, ApJ, 187, 425
Rozo E., Rykoff E., Koester B., Nord B., Wu H.-Y., Evrard A., Wechsler R., 2011, ApJ, 740, 53
Rozo E. et al., 2009a, ApJ, 699, 768
Rozo E. et al., 2009b, ApJ, 703, 601
Rykoff E. S. et al., 2014, ApJ, 785, 104
Rykoff E. S. et al., 2016, ApJs, 224, 1
Sánchez-Blázquez P. et al., 2006, MNRAS, 371, 703
Sevilla I. et al., 2011, preprint (arXiv:astro-ph/1109.6741)
Sheth R. K., Tormen G., 2002, MNRAS, 329, 61
Simet M., McClintock T., Mandelbaum R., Rozo E., Rykoff E., Sheldon E., Wechsler R. H., 2017, MNRAS, 466, 3103
Simha V., Weinberg D. H., Conroy C., Dave R., Fardal M., Katz N., Oppenheimer B. D., 2014, ArXiv e-prints
Soares-Santos M. et al., 2011, ApJ, 727, 45
Taylor E. N. et al., 2011, MNRAS, 418, 1587
Taylor M. B., 2005, in Astronomical Society of the Pacific Conference Series, Vol. 347, Astronomical Data Analysis Software and Systems XIV, Shopbell P., Britton M., Ebert R., eds., p. 29
The Dark Energy Survey Collaboration, 2005, preprint (arXiv:astro-ph/0510346)

Tinker J., Kravtsov A. V., Klypin A., Abazajian K., Warren M., Yepes G., Gottlöber S., Holz D. E., 2008, ApJ, 688, 709
Wechsler R. H., Tinker J. L., 2018, ARA&A, 56, 435
Welch B., Annis J., Li H., Palmese A., Soares-Santos M., 2019, in prep.
Zhang Y. et al., 2017, arXiv e-prints
Zu Y., Mandelbaum R., 2016, MNRAS, 457, 4360

6 AFFILIATIONS

[1] Fermi National Accelerator Laboratory, P. O. Box 500, Batavia, IL 60510, USA
[2] Department of Physics & Astronomy, University College London, Gower Street, London, WC1E 6BT, UK
[3] Department of Astronomy, The Ohio State University, Columbus, OH 43210, USA
[4] Department of Physics, Carnegie Mellon University, Pittsburgh, Pennsylvania 15312, USA
[5] Brandeis University, Physics Department, 415 South Street, Waltham MA 02453
[6] Kavli Institute for Cosmological Physics, University of Chicago, Chicago, IL 60637, USA
[7] Department of Physics and Astronomy, Pevensey Building, University of Sussex, Brighton, BN1 9QH, UK
[8] Santa Cruz Institute for Particle Physics, Santa Cruz, CA 95064, USA
[9] Department of Astronomy, University of Michigan, Ann Arbor, MI 48109, USA
[10] Department of Physics, University of Michigan, Ann Arbor, MI 48109, USA
[11] Astrophysics & Cosmology Research Unit, School of Mathematics, Statistics & Computer Science, University of KwaZulu-Natal, Westville Campus, Durban 4041, South Africa
[12] Department of Physics, Stanford University, 382 Via Pueblo Mall, Stanford, CA 94305, USA
[13] Kavli Institute for Particle Astrophysics & Cosmology, P. O. Box 2450, Stanford University, Stanford, CA 94305, USA
[14] SLAC National Accelerator Laboratory, Menlo Park, CA 94025, USA
[15] Department of Physics, ETH Zurich, Wolfgang-Pauli-Strasse 16, CH-8093 Zurich, Switzerland
[16] New York University, CCPP, New York, NY 10003, USA
[17] Department of Physics, University of Arizona, Tucson, AZ 85721, USA
[18] Max Planck Institute for Extraterrestrial Physics, Giessenbachstrasse, 85748 Garching, Germany
[19] Universitäts-Sternwarte, Fakultät für Physik, Ludwig-Maximilians Universität München, Scheinerstr. 1, 81679 München, Germany
[20] Institute of Cosmology and Gravitation, University of Portsmouth, Portsmouth, PO1 3FX, UK
[21] Centro de Investigaciones Energéticas, Medioambientales y Tecnológicas (CIEMAT), Madrid, Spain
[22] Laboratório Interinstitucional de e-Astronomia - LIneA, Rua Gal. José Cristino 77, Rio de Janeiro, RJ - 20921-400, Brazil
[23] Department of Astronomy, University of Illinois at Urbana-Champaign, 1002 W. Green Street, Urbana, IL 61801, USA
[24] National Center for Supercomputing Applications, 1205 West Clark St., Urbana, IL 61801, USA
[25] Institut de Física d'Altes Energies (IFAE), The Barcelona Institute of Science and Technology, Campus UAB, 08193 Bellaterra (Barcelona) Spain
[26] Institut d'Estudis Espacials de Catalunya (IEEC), 08034 Barcelona, Spain
[27] Institute of Space Sciences (ICE, CSIC), Campus UAB, Carrer de Can Magrans, s/n, 08193 Barcelona, Spain

[28] Astrophysics Research Institute, Liverpool John Moores University, IC2, Liverpool Science Park, 146 Brownlow Hill, Liverpool, L3 5RF, UK
[29] Observatório Nacional, Rua Gal. José Cristino 77, Rio de Janeiro, RJ - 20921-400, Brazil
[30] Department of Physics, IIT Hyderabad, Kandi, Telangana 502285, India
[31] Excellence Cluster Origins, Boltzmannstr. 2, 85748 Garching, Germany
[32] Faculty of Physics, Ludwig-Maximilians-Universität, Scheinerstr. 1, 81679 Munich, Germany
[33] Instituto de Fisica Teorica UAM/CSIC, Universidad Autonoma de Madrid, 28049 Madrid, Spain
[34] Center for Cosmology and Astro-Particle Physics, The Ohio State University, Columbus, OH 43210, USA
[35] Department of Physics, The Ohio State University, Columbus, OH 43210, USA
[36] Harvard-Smithsonian Center for Astrophysics, Cambridge, MA 02138, USA
[37] Department of Astronomy/Steward Observatory, University of Arizona, 933 North Cherry Avenue, Tucson, AZ 85721-0065, USA
[38] Australian Astronomical Optics, Macquarie University, North Ryde, NSW 2113, Australia
[39] Institute for Astronomy, University of Edinburgh, Royal Observatory, Blackford Hill, Edinburgh, EH9 3HJ, UK
[40] Departamento de Física Matemática, Instituto de Física, Universidade de São Paulo, CP 66318, São Paulo, SP, 05314-970, Brazil
[41] Institute for Astronomy, University of Edinburgh, Royal Observatory, Blackford Hill, Edinburgh EH9 3NJ
[42] George P. and Cynthia Woods Mitchell Institute for Fundamental Physics and Astronomy, and Department of Physics and Astronomy, Texas A&M University, College Station, TX 77843, USA
[43] Institució Catalana de Recerca i Estudis Avançats, E-08010 Barcelona, Spain
[44] Department of Astrophysical Sciences, Princeton University, Peyton Hall, Princeton, NJ 08544, USA
[45] BIPAC, Department of Physics, University of Oxford, Denys Wilkinson Building, 1 Keble Road, Oxford OX1 3RH, UK
[46] Instituto de Física Gleb Wataghin, Universidade Estadual de Campinas, 13083-859, Campinas, SP, Brazil
[47] Sub-department of Astrophysics, Department of Physics, University of Oxford, Denys Wilkinson Building, Keble Road, Oxford OX1 3RH, UK and Department of Physics, Lancaster University, Lancaster LA1 4 YB, UK
[48] Computer Science and Mathematics Division, Oak Ridge National Laboratory, Oak Ridge, TN 37831
[49] Departamento de Física e Astronomia, Faculdade de Ciencias, Universidade do Porto, Rua do Campo Alegre, 687, P-4169-007 Porto, Portugal
[50] Instituto de Astrofísica e Ciencias do Espaco, Universidade do Porto, CAUP, Rua das Estrelas, P-4150-762 Porto, Portugal
[51] Argonne National Laboratory, 9700 South Cass Avenue, Lemont, IL 60439, USA
[52] Cerro Tololo Inter-American Observatory, National Optical Astronomy Observatory, Casilla 603, La Serena, Chile

This document was prepared by [DES Collaboration] using the resources of the Fermi National Accelerator Laboratory (Fermilab), a U.S. Department of Energy, Office of Science, HEP User Facility. Fermilab is managed by Fermi Research Alliance, LLC (FRA), acting under Contract No. DE-AC02-07CH11359.